Research Square

Preprints are preliminary reports that have not undergone peer review.
They should not be considered conclusive, used to inform clinical practice,
or referenced by the media as validated information.

Measurement-Informed Multi-spin Photonic Ising Relaxation in a Single Spiral TCSEL

Salem Altaleb
Abdolah Amirany
Mohammad Jooq
Luke Graham
Pritha Khurana
Jim Tatum
Jim Guenter
Eric Du
Hamed Dalir
hamed.dalir@ufl.edu

Univeristy of Florida https://orcid.org/0000-0002-9998-3830

Article

Keywords: Photonic Ising Machine, Spiral TCSEL, Optical Computing, Photonic Annealing, Combinatorial Optimization

Posted Date: November 20th, 2026

DOI: https://doi.org/10.21203/rs.3.rs-10562696/v1

License: This work is licensed under a Creative Commons Attribution 4.0 International License.
Read Full License

Additional Declarations: There is **NO** Competing Interest.

Measurement-Informed Multi-spin Photonic Ising Relaxation in a Single Spiral TCSEL

Salem Altaleb[1], Abdolah Amirany[1], Mohammad K. Q. Jooq[2], Luke Graham[3], Pritha Khurana[3], Jim Tatum[3], Jim Guenter[3], Eric Jing Du[4], Hamed Dalir[1*]

[1]Department of Electrical and Computer Engineering, University of Florida, Gainesville, 32611, FL, USA.
[2]School of Built Environment, Engineering and Computing, Leeds Beckett University, Leeds, LS1 3HB, West Yorkshire, UK.
[3]Dallas Quantum Devices, Inc, Allen, 75013, TX, United States.
[4]Department of Civil and Coastal Engineering, University of Florida, Gainesville, 32611, FL, USA.

*Corresponding author(s). E-mail(s): hamed.dalir@ufl.edu;

Abstract

Physical Ising machines offer a route to solving combinatorial optimization problems through the natural relaxation of interacting states, but many photonic implementations require replicated optical units or external coupling networks. Here, we introduce SPIRA, a multi-spin photonic Ising relaxation architecture based on a single spiral transverse-cavity surface-emitting laser (TCSEL). The model is informed by measured multimode spectra, current-dependent optical output, and temperature-dependent near-field distributions of the fabricated device. These measurements provide the modal amplitudes and spatial information used to construct a 16-spin effective Hamiltonian, in which spin interactions arise from geometry-defined modal coupling and amplitude weighting, while local fields are represented through gain–loss imbalance. The TCSEL-mapped Hamiltonian achieves 87.5% spin agreement with the target ground state and a relative energy error of 6.42%. In application benchmarks, SPIRA reaches 96.90% of the optimal Max-Cut value, exactly recovers the optimum number partition, and obtains 87.50% agreement with the optimal QUBO solution, with an 18.26% objective gap. Monte Carlo analysis further shows robust near-ground-state recovery under coupling mismatch and device-level perturbations. These results establish measurement-informed

multimode TCSEL dynamics as a compact platform for device-level photonic Ising relaxation.

Keywords: Photonic Ising Machine, Spiral TCSEL, Optical Computing, Photonic Annealing, Combinatorial Optimization

1 Introduction

Combinatorial optimization problems arise in graph theory, logistics, scheduling, machine learning, and network design, where the objective is to identify favorable configurations within exponentially large solution spaces [1–3]. Many such problems are computationally difficult because their energy landscapes contain competing constraints and numerous local minima [4]. The Ising and quadratic unconstrained binary optimization (QUBO) formulations provide a common representation for these problems by encoding binary variables through pairwise interactions and local biases [3, 5, 6]. This representation enables optimization problems to be mapped onto physical systems whose intrinsic dynamics drive them toward low-energy configurations [1, 7, 8].

Physical Ising machines have been realized using electronic, photonic, spintronic, and quantum platforms. CMOS annealing processors and coupled-oscillator networks provide room-temperature operation and compatibility with integrated electronics, but dense or arbitrary coupling graphs can require substantial routing and control overhead [9–11]. Spintronic implementations exploit the stochastic dynamics of magnetic devices and offer compact binary elements, although large interaction networks introduce interconnect, variability, and readout challenges [12]. Quantum annealers provide programmable Ising Hamiltonians using superconducting qubits, but require cryogenic operation, specialized control infrastructure, and graph embedding [13]. These trade-offs motivate physical solvers that combine compact integration, room-temperature operation, and intrinsic interaction dynamics.

Photonic Ising machines are particularly attractive because optical systems support high-bandwidth propagation, coherent interference, parallel evolution, and low-latency analog relaxation [6, 14, 15]. Coherent Ising machines have demonstrated large spin networks using time-multiplexed optical pulses, while recent spatial, optoelectronic, and integrated implementations have improved programmability and Hamiltonian evaluation [8, 16–19]. However, many of these architectures construct the interaction network through delay lines, measurement-feedback loops, external coupling controllers, or replicated optical units. Spatial implementations can additionally face coupling-precision, matrix-rank, and integration-density constraints [1, 20]. Consequently, the spin states and their interactions are often distributed across a system-level architecture rather than embedded within a single compact optical device.

Transverse-cavity surface-emitting lasers (TCSELs) provide a promising device-level alternative because they combine compact emission, high-speed operation, nonlinear optical dynamics, and compatibility with dense integration [21, 22]. Their polarization dynamics, optical feedback, gain competition, and transverse-mode

interactions enable complex collective behavior within one semiconductor cavity [23–25]. In large-area and structured-aperture devices, spatial-hole burning, thermal detuning, and aperture-dependent confinement redistribute optical power among multiple transverse modes [25–27]. These properties suggest that a single multimode TCSEL can act as an analog relaxation system in which several effective states and their interactions coexist within the same physical cavity. Nevertheless, the use of multimode spiral-TCSEL dynamics to represent multiple interacting Ising spins within one device remains largely unexplored.

Here, we introduce SPIRA, a multi-spin photonic Ising relaxation architecture based on a single spiral TCSEL. The model is informed by measured multimode emission spectra, current-dependent optical output, and temperature-dependent near-field intensity distributions of the fabricated device. The spiral aperture is discretized into $N = 16$ effective optical spin sites, while the measured modal amplitudes and geometry-dependent overlap are used to construct the effective interaction network. Pairwise Ising coupling is represented through geometry-defined modal interaction and amplitude weighting, whereas the local-field term is associated with the modal gain–loss imbalance. In this way, the same TCSEL cavity supports the effective spin states, interaction backbone, and relaxation landscape without requiring one replicated physical device for each spin.

The measurement-informed TCSEL Hamiltonian achieves 87.5% ground-state spin agreement with the target Ising model and a relative energy error of 6.42%. In optimization benchmarks, SPIRA reaches 96.90% of the exact Max-Cut value, recovers the optimal number partition with zero objective gap, and reproduces 87.50% of the optimal QUBO binary variables. Monte Carlo analysis further demonstrates near-ground-state recovery under coupling mismatch, local-field uncertainty, and device-level perturbations. These results establish the multimode dynamics of a single spiral TCSEL as a compact physical substrate for multi-spin photonic Ising relaxation.

The rest of this paper is organized as follows. Section 2 introduces the spiral-TCSEL device concept and discusses the optical modal behavior that motivates its use as a physical relaxation substrate. Section 3 presents the Ising-machine formulation, including binary spins, pairwise couplings, local fields, and Hamiltonian minimization. Section 4 introduces the SPIRA mapping, relating the optical modal states, geometry-defined coupling, amplitude redistribution, and gain–loss biasing to the effective Ising Hamiltonian. Section 5 presents the experimental characterization and computational evaluation, including Hamiltonian mapping, energy-landscape analysis, Monte Carlo robustness, and optimization benchmarks. Finally, Section 6 summarizes the main findings and outlines future directions for scalable spiral-TCSEL Ising hardware.

2 Spiral-TCSEL Device

2.1 Device Architecture

The device investigated in this work was fabricated using a standard 850-nm high-power oxide-confined TCSEL epitaxial platform. The vertical cavity consists of a bottom distributed Bragg reflector (DBR), a multiple-quantum-well active region,

an oxidized current-confinement layer, and a top DBR. Electrical injection is provided through a patterned top p-type contact and a bottom n-type contact, preserving vertical emission while defining the lateral current path [28–30]. Unlike a conventional circular-aperture device, the top electrode and active emission region follow an Archimedean spiral trajectory. The spiral centerline is described by Eq. 1.

$$r(\phi) = r_0 + a\phi, \tag{1}$$

where r_0 is the initial radius, a determines the radial pitch, and ϕ is the azimuthal coordinate. The corresponding lateral path length is defined using Eq. 2.

$$L_{\mathrm{sp}} = \int_{\phi_0}^{\phi_1} \sqrt{r^2(\phi) + \left(\frac{dr(\phi)}{d\phi}\right)^2}\, d\phi, \tag{2}$$

where ϕ_0 and ϕ_1 define the angular extent of the spiral. Relative to a circular aperture of comparable footprint, this geometry extends the interaction path among the injected carriers, optical field, and distributed cavity feedback. Related transverse-coupled-cavity devices have shown that lateral cavity shaping and optical feedback can strongly modify modal dynamics, spectral response, and modulation behavior [31–33].

As illustrated in Fig. 1, the structure can be viewed as a vertically emitting Bragg-reflector waveguide following a curved in-plane trajectory. The top DBR provides output coupling, the bottom DBR provides high-reflectivity feedback, and the quantum-well region supplies optical gain. The oxide aperture confines the injected current and contributes to transverse-mode formation, while the patterned p-contact defines the spiral excitation path [28–30].

2.2 Device-native Modal Interaction

The spiral geometry modifies both the spatial overlap and the relative phase of the supported transverse optical fields. Repeated reflection between the upper and lower DBRs, together with propagation along the curved aperture, creates a distributed zig-zag interaction path. This configuration combines lateral modal interaction with vertical emission and can modify gain competition, mode filtering, and cavity feedback [31, 34–36]. For two complex transverse fields $E_i(\mathbf{r})$ and $E_j(\mathbf{r})$, the normalized complex overlap over the active spiral region is defined using Eq. 3.

$$\widetilde{\kappa}_{ij}^{\mathrm{sp}} = \frac{\displaystyle\int_{\Omega_{\mathrm{sp}}} E_i^*(\mathbf{r}) E_j(\mathbf{r})\, d\mathbf{r}}{\sqrt{\displaystyle\int_{\Omega_{\mathrm{sp}}} |E_i(\mathbf{r})|^2\, d\mathbf{r} \int_{\Omega_{\mathrm{sp}}} |E_j(\mathbf{r})|^2\, d\mathbf{r}}} = \left|\widetilde{\kappa}_{ij}^{\mathrm{sp}}\right| e^{\mathrm{i}\theta_{ij}}, \tag{3}$$

where Ω_{sp} denotes the active spiral region. The magnitude $\left|\widetilde{\kappa}_{ij}^{\mathrm{sp}}\right|$ quantifies the interaction strength, whereas θ_{ij} represents the relative phase accumulated through propagation, reflection, interference, and cavity detuning. Retaining this complex form

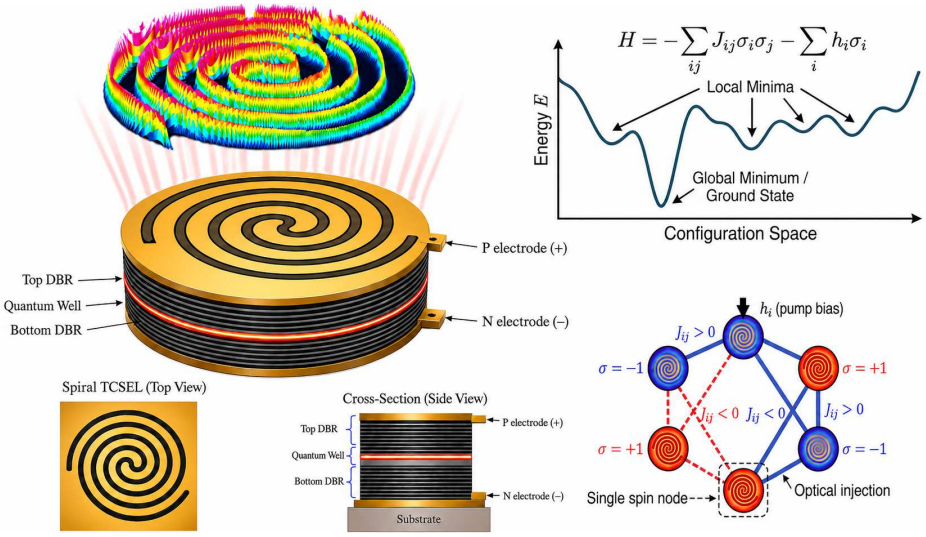

Fig. 1: Spiral-TCSEL architecture and device-native Ising concept. The schematic shows the spiral top contact, oxide-confined active region, upper and lower distributed Bragg reflectors, lateral zig-zag optical-interaction path, vertical emission, and multiple effective optical sites supported within a single cavity.

is important because a magnitude-only overlap cannot distinguish interaction channels with different phase preferences. A signed phase-sensitive interaction coefficient can therefore be written using Eq. 4.

$$\kappa_{ij}^{\mathrm{sp}} = \mathrm{Re}\left[\widetilde{\kappa}_{ij}^{\mathrm{sp}}\right] = \left|\widetilde{\kappa}_{ij}^{\mathrm{sp}}\right| \cos\theta_{ij}. \tag{4}$$

Positive and negative values of $\kappa_{ij}^{\mathrm{sp}}$ correspond to interaction channels favoring different relative optical phases. The spiral geometry thus establishes a structured, device-native interaction backbone, while changes in modal amplitudes under electrical or thermal tuning modify the effective interaction strengths. This combination of geometry-defined coupling and operating-condition-dependent modal redistribution provides the physical basis for the Ising mapping developed in Section 4.

3 Ising Optimization Framework

The Ising model represents a system of N binary variables, $\sigma_i \in \{-1, +1\}$, through pairwise interactions and local biases. Its Hamiltonian is written using Eq. 5 [5, 6].

$$H(\boldsymbol{\sigma}) = -\sum_{i<j} J_{ij}\sigma_i\sigma_j - \sum_{i=1}^{N} h_i\sigma_i, \tag{5}$$

where J_{ij} denotes the interaction strength between spins i and j, and h_i is the local field acting on spin i. Under this sign convention, $J_{ij} > 0$ favors aligned spins, whereas

$J_{ij} < 0$ favors anti-aligned spins. The local field breaks the symmetry between the two spin states and introduces a preference for $\sigma_i = +1$ or $\sigma_i = -1$, depending on the sign of h_i. The associated optimization problem is the determination of the ground-state configuration of Eq. 6.

$$\boldsymbol{\sigma}^* = \underset{\boldsymbol{\sigma}\in\{-1,+1\}^N}{\arg\min} \; H(\boldsymbol{\sigma}), \tag{6}$$

which corresponds to the minimum of the Ising energy landscape. For N spins, this landscape contains 2^N possible configurations and can include multiple local minima and degenerate or nearly degenerate ground states [2, 4]. Consequently, optimization quality is more appropriately assessed using the obtained energy or objective value than by comparison with only one selected ground-state configuration. Many binary optimization problems are initially expressed in quadratic unconstrained binary optimization form of Eq. 7.

$$E_{\mathrm{Q}}(\boldsymbol{x}) = \boldsymbol{x}^{\mathrm{T}}\mathbf{Q}\boldsymbol{x}, \qquad x_i \in \{0, 1\}, \tag{7}$$

where $\mathbf{Q}$ contains the linear and quadratic problem coefficients [3, 37]. The binary and Ising variables are related through Eq. 8.

$$x_i = \frac{1 + \sigma_i}{2}, \qquad \sigma_i = 2x_i - 1. \tag{8}$$

Substituting Eq. 8 into Eq. 7 and collecting the linear and quadratic spin terms produces an equivalent Ising Hamiltonian of the form given in Eq. 5, up to an additive constant that does not affect the minimizing configuration [3, 5]. The Ising representation therefore provides a common interface for graph-partitioning, number-partitioning, and general QUBO problems.

A physical Ising machine realizes this mathematical model by associating each spin with a measurable physical degree of freedom and embedding J_{ij} and h_i into the interactions and biases of the underlying system [6, 14]. After initialization, the system evolves through deterministic relaxation, stochastic transitions, or a combination of both toward a stable low-energy configuration. The final state is then decoded as a candidate solution rather than being assumed to be the exact ground state in every realization. In SPIRA, these quantities are mapped onto the multimode states, phase-sensitive interactions, modal amplitudes, and gain–loss dynamics of the spiral TCSEL, as developed in Section 4.

4 Mapping the Spiral-TCSEL to an Effective Ising Model

SPIRA maps the multimode response of a single spiral-TCSEL onto an effective Ising Hamiltonian. The spiral geometry provides a structured interaction network, while electrical and thermal tuning modifies the modal amplitudes and gain–loss landscape. The measured spectrum, light–current response, and temperature-dependent near-field distributions constrain the model. In contrast, the binary phase states, signed couplings, and mode-dependent local fields are represented at the modeling level.

4.1 Effective Spin Representation

The spiral aperture is discretized into N effective optical sites, with $N = 16$ used in the present implementation. The complex optical field associated with site i is written using Eq. 9.

$$E_i = A_i e^{j\phi_i}, \tag{9}$$

where A_i and ϕ_i denote the modal amplitude and phase, respectively. The normalized amplitude A_i is extracted from the measured near-field intensity within each segmented region.

The Ising spin is represented using two optical phase states. The states $\phi_i = 0$ and $\phi_i = \pi$ correspond to $\sigma_i = +1$ and $\sigma_i = -1$, respectively. The relative phase therefore determines whether two optical states are aligned or anti-aligned. Because the present near-field measurements provide intensity rather than phase, the binary phases are treated as model variables. Direct experimental spin readout would require phase-resolved near-field or interferometric measurements.

4.2 Measurement-Informed Coupling

The interaction between two optical sites is determined by their spatial overlap, propagation phase, cavity feedback, and shared gain dynamics. The signed coupling coefficient introduced in Section 2 provides the device-native interaction backbone. Its sign distinguishes optical interactions that favor different relative phase states. The effective Ising coupling is defined using Eq. 10.

$$J_{ij}^{\text{eff}} = \kappa_{ij}^{\text{sp}} A_i A_j, \tag{10}$$

where κ_{ij}^{sp} is primarily determined by the fabricated spiral geometry and $A_i A_j$ provides amplitude-dependent weighting. The geometry therefore defines the fixed coupling structure, while the measured redistribution of optical intensity under current and temperature tuning modifies the effective interaction strength.

The present device consequently realizes a structured coupling family rather than an independently programmable arbitrary coupling matrix. Different Ising problems are approximated by adjusting the modal-amplitude distribution within this device-native interaction structure.

4.3 Gain–Loss-Based Local Fields

The local field represents the preference of an individual optical site for one binary state. In SPIRA, this preference is associated with the balance between modal gain and modal loss of Eq. 11.

$$h_i^{\text{eff}} = g_i - \gamma_i, \tag{11}$$

where g_i represents the effective modal gain and γ_i represents the corresponding modal loss. Gain is influenced by injection current, carrier density, and temperature, whereas loss depends on cavity detuning, DBR response, wavelength, emission angle, and photon lifetime. The controllability of the mapped Ising parameters is summarized in Table 1.

Table 1: Controllable parameters in the spiral-TCSEL Ising mapping

Parameter	TCSEL meaning	Controllability	Control mechanism
σ_i	Binary optical phase or dominant modal state	Indirectly controllable	Current and temperature
A_i	Modal amplitude	Controllable	Injection current, carrier density, gain saturation, and thermal shift
g_i	Modal gain	Controllable	Injection current, carrier density, and temperature
γ_i	Modal loss	Partially controllable	Wavelength, photon lifetime, and thermal detuning
h_i^{eff}	Net modal bias	Controllable	Gain–loss balance and temperature
κ_{ij}	Bare modal coupling	Mostly fixed	Geometry, aperture profile, modal overlap, and cavity design
J_{ij}^{eff}	Effective coupling	Partially controllable	Modal amplitude redistribution
λ_i	Modal wavelength	Indirectly controllable	Temperature and cavity resonance
$\tau_{\mathrm{ph},i}$	Photon lifetime	Partially controllable	Wavelength, polarization, DBR reflectivity, and emission angle
Annealing	Relaxation trajectory	Controllable	Current and temperature

The light–current measurements determine the threshold and global operating condition of the device, while the near-field measurements reveal the corresponding spatial redistribution of optical power. Because conventional light–current measurements are not spatially resolved, the individual values of g_i, γ_i, and h_i^{eff} are effective modeled quantities rather than direct measurements. Current and temperature nevertheless provide practical controls for modifying the overall gain–loss landscape. At a selected current and temperature, the competing transverse modes evolve through optical interference, gain saturation, carrier redistribution, and cavity loss. The resulting stable modal configuration is interpreted as a low-energy state of the effective Ising Hamiltonian. In the present work, this relaxation and the corresponding spin readout are evaluated numerically using the measurement-informed model.

5 Results and Discussion

This section evaluates SPIRA from experimental characterization to computational performance. First, the measured emission spectrum, current-dependent optical output, and temperature-dependent near-field distributions are used to characterize the multimode response and extract the effective optical spin sites. Next, the measurement-informed TCSEL Hamiltonian is evaluated through spin-state, coupling, local-field, and energy-landscape comparisons. Monte Carlo simulations are then used to assess robustness against coupling mismatch, local-field uncertainty, and device-level

perturbations. Finally, the computational performance is examined using Max-Cut, number-partitioning, and QUBO benchmarks and compared with representative Ising-machine implementations.

5.1 Experimental TCSEL Measurement

The device under test is a spiral-aperture TCSEL with a 1 mm × 1 mm emission aperture. The laser was biased using a Keysight B2910BL precision source/measure unit. The device was mounted in an Arroyo Instruments 207 TEC laser mount, and its temperature was stabilized using an Arroyo Instruments TECSource 5240 (4 A/7 V) controller. The spatial measurements were performed at a fixed drive current above threshold. Near-field data were acquired at 25°C, 45°C, 65°C, and 85°C using the same electrical and thermal control chain, ensuring matched operating conditions.

The optical spectrum was recorded using a Yokogawa AQ6370D optical spectrum analyzer. The emission was collected using a multimode lensed optical probe with a 50 µm core, providing a focused spot size of approximately 25 µm at the device facet. As shown in Fig. 2a, the measured spectrum contains multiple peaks over the lasing wavelength range, confirming that several optical modes are simultaneously supported by the spiral cavity. This multimode operation is essential to the proposed Ising mapping because the effective spin states and their interactions are represented by multiple optical degrees of freedom within the same cavity.

Figure 2b shows the normalized optical output power as a function of bias current at different temperatures. These measurements identify the threshold and operating range of the device and provide the global current–temperature conditions used to constrain the gain–loss landscape of the effective Ising model.

The near-field intensity distribution was imaged using a DataRay TaperCamD-LCM CMOS beam-profiling camera with 2048 × 2048 pixels. The effective sample-plane pixel pitch was calibrated against a reference target, yielding 6.0317 µm per pixel and a corresponding field of view of 12.35 mm. Raw frames were background-corrected by subtracting a fixed dark level before analysis; no spatial denoising was applied.

Figures 2d–2g show the normalized near-field distributions as three-dimensional surface renderings. The measurements reveal the temperature-dependent evolution of the transverse modal structure across the spiral aperture. The background-corrected intensity within each of the $N = 16$ segmented optical sites was used to extract the modal-amplitude distribution A_i employed in the coupling-matrix mapping of Sec. 5.2.

5.2 TCSEL-Mapped Hamiltonian Results

The numerical benchmark was performed by discretizing the spiral aperture into $N = 16$ effective optical spin sites, giving 2^{16} possible spin configurations for each Hamiltonian. For each case, the target Ising Hamiltonian and the corresponding TCSEL-mapped Hamiltonian were constructed using the same spin basis, enabling a direct state-by-state comparison between the reference Ising model and the measurement-informed mapping. The target coupling matrix J_{ij}^{target} defines the reference optimization problem, whereas the mapped Hamiltonian uses

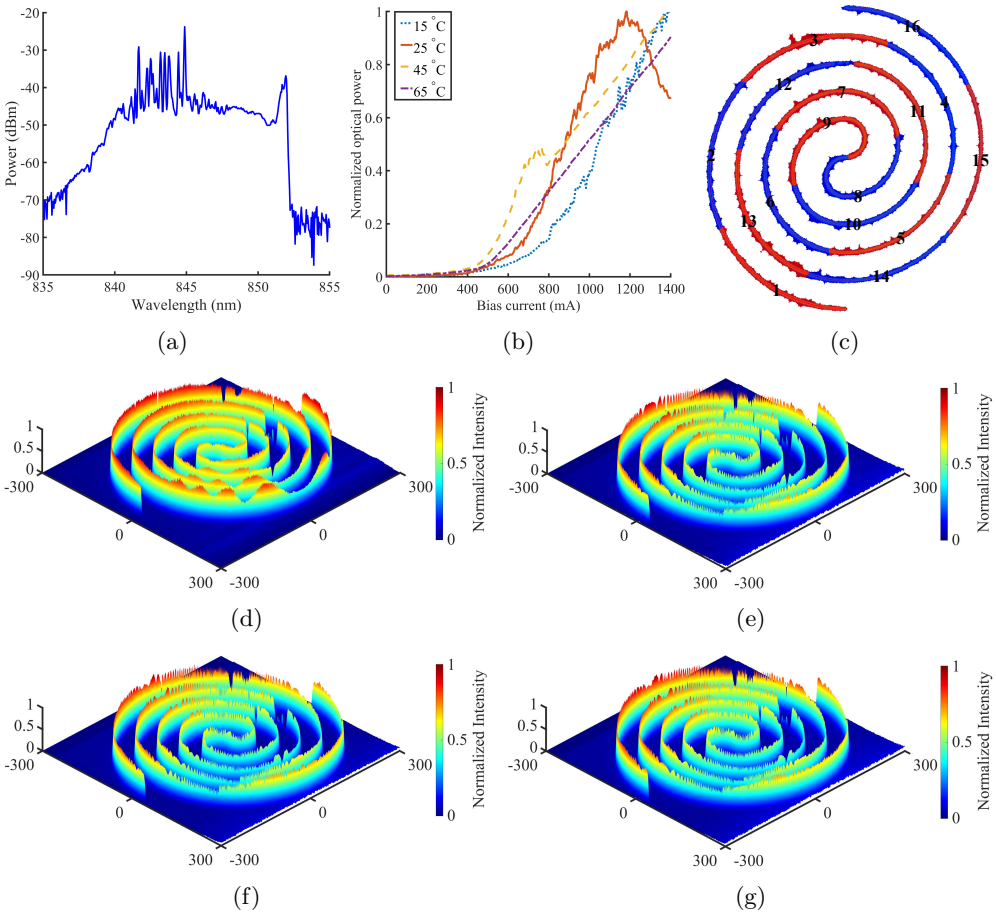

Fig. 2: Optical characterization and spin-site extraction of the spiral TCSEL. (a) Measured emission spectrum showing multimode lasing operation. (b) Normalized optical output power as a function of bias current at temperatures of 15°C, 25°C, 45°C, and 65°C. (c) Segmentation of the spiral aperture into $N = 16$ effective spin sites, with red and blue regions representing the two binary spin states. (d)–(g) Normalized three-dimensional near-field intensity distributions measured at 25°C, 45°C, 65°C, and 85°C, respectively.

the geometry-defined spiral coupling $\kappa_{ij}^{\mathrm{sp}}$, modal-amplitude weighting $A_i A_j$, and gain–loss-based local field h_i^{eff}. The ground state of each Hamiltonian was obtained by evaluating the complete configuration space.

Figures 3a–3c compare the ground-state configurations obtained from the target and TCSEL-mapped Hamiltonians. The mapped ground state is obtained after replacing the target coupling and local-field terms with the effective TCSEL parameters. The comparison therefore tests whether the spiral-TCSEL mapping

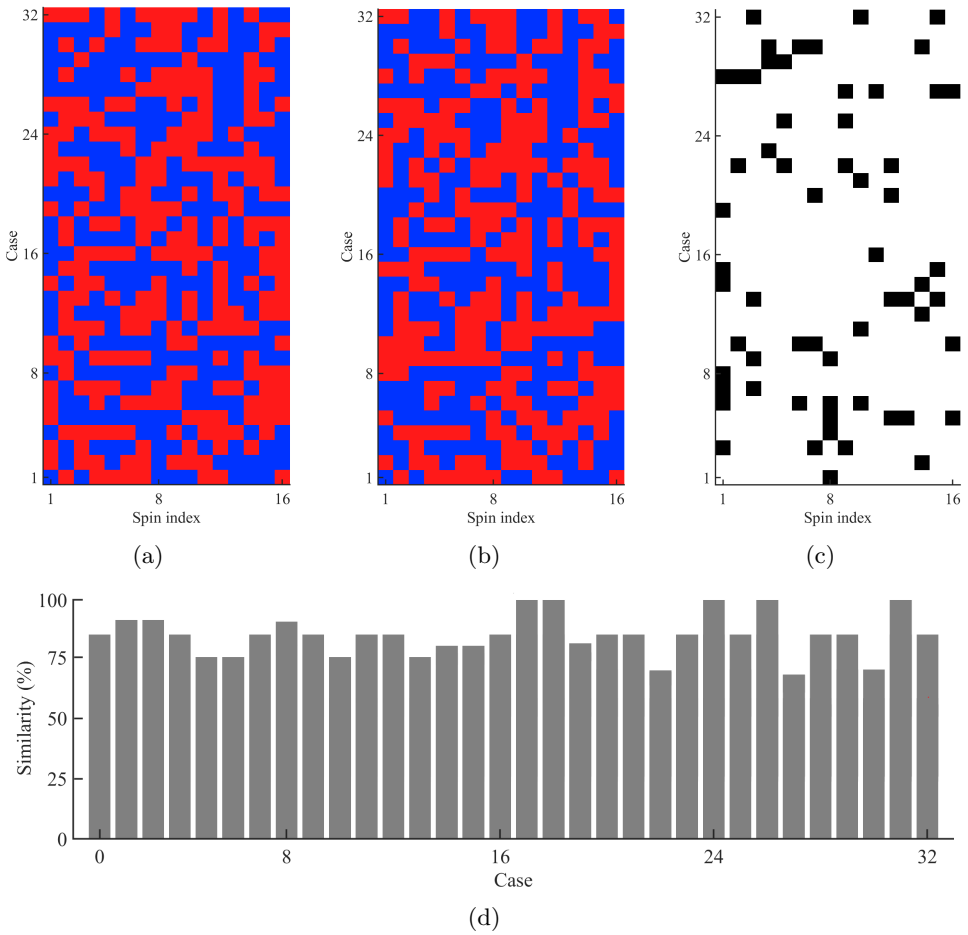

Fig. 3: Comparison of the target and TCSEL-mapped spin configurations. (a) Target ground state. (b) TCSEL-mapped ground state. (c) Spin-mismatch map. (d) Ground-state similarity across the evaluated benchmark cases.

preserves the low-energy solution structure of the original Ising problem. The mapped model reproduces most of the target spin configuration, with mismatches confined to a limited number of sites.

To quantify this agreement, the spin similarity was calculated over multiple benchmark cases by comparing the target and TCSEL-mapped ground-state vectors. As shown in Fig. 3d, the similarity remains high across the evaluated cases, indicating that the mapped Hamiltonian preserves the relevant low-energy spin structure despite deviations in the effective coupling and local-field parameters. Because degenerate or near-degenerate configurations can represent equivalent solutions, the spin similarity is considered together with the achieved energy and objective value.

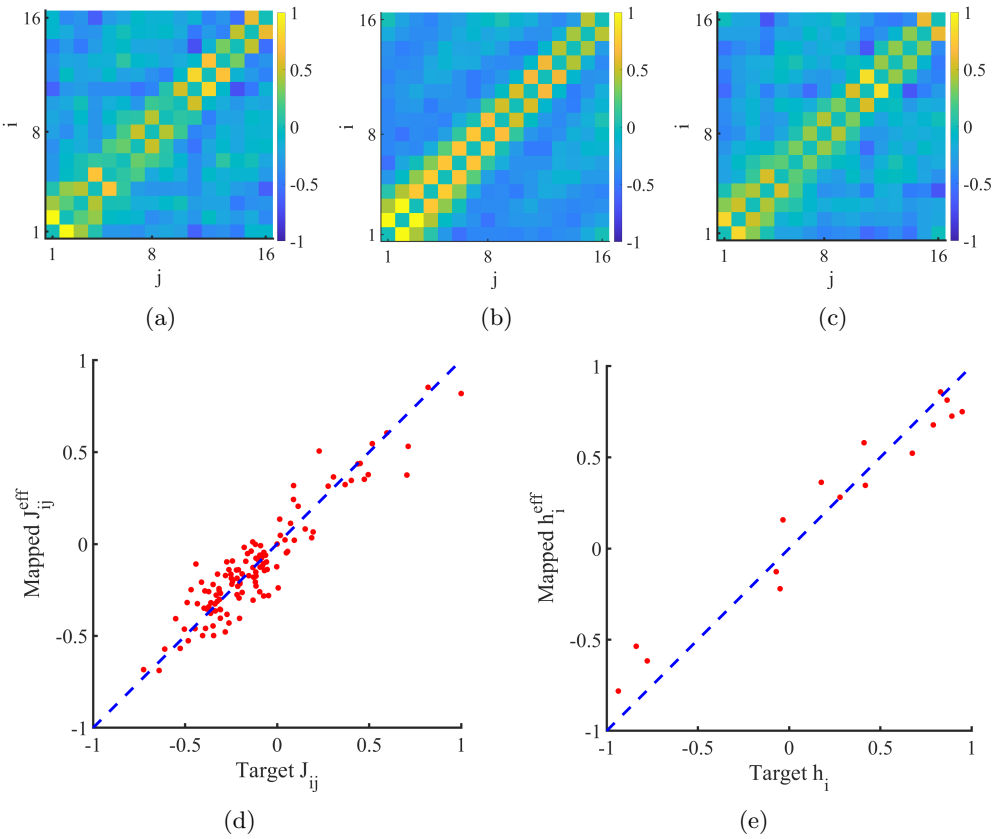

Fig. 4: Coupling and local-field mapping. (a) Target coupling matrix J_{ij}^{target}. (b) Geometry-defined spiral coupling matrix κ_{ij}^{sp}. (c) Effective TCSEL coupling matrix J_{ij}^{eff}. (d) Correlation between the target and TCSEL-mapped coupling values. (e) Correlation between the target and TCSEL-mapped local fields.

For the representative $N = 16$ benchmark, the target Ising Hamiltonian reaches a minimum energy of -15.1251, while the TCSEL-mapped spin configuration gives an energy of -14.1544 when evaluated using the target Hamiltonian. This corresponds to a relative energy error of 6.42%. The ground-state spin agreement is 87.50%, showing that most spin variables are recovered despite the constraints imposed by the physical coupling structure of the spiral TCSEL. The parameter-level errors further clarify the origin of this deviation. The relative coupling error is 34.21%, reflecting that J_{ij}^{eff} is derived from the geometry-defined coupling κ_{ij}^{sp} and amplitude weighting $A_i A_j$, rather than being independently programmed. The relative local-field error is 23.69%, representing the imperfect realization of the target bias through the gain–loss term $g_i - \gamma_i$. The amplitude-fitting loss is 8.70%, indicating that modal-amplitude weighting improves the correspondence between the TCSEL-mapped and target Hamiltonians.

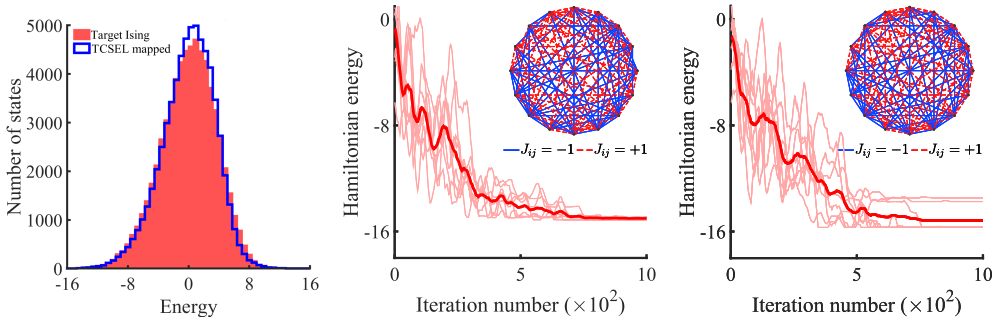

Fig. 5: Energy-landscape and numerical-relaxation comparison. (a) Energy distributions of the target and TCSEL-mapped Hamiltonians. (b) Energy trajectories of the target Ising Hamiltonian during stochastic annealing. (c) Energy trajectories of the TCSEL-mapped Hamiltonian under the same numerical relaxation procedure ($J_{ij} = -1$, blue; $J_{ij} = +1$, red).

The coupling structure of the benchmark problem is first defined by the target Ising Hamiltonian. Figure 4a shows J_{ij}^{target}, which represents the desired pairwise interaction network among the effective spins. Positive and negative entries favor aligned and anti-aligned spin configurations, respectively, under the sign convention introduced in Sec. 3. The physical coupling available in the spiral TCSEL is determined primarily by the device geometry. As shown in Fig. 4b, the bare coupling matrix κ_{ij}^{sp} is imposed by the spiral aperture, modal overlap, optical path length, and phase-sensitive interference among the supported optical states. It therefore forms the device-native interaction backbone rather than an externally programmed arbitrary matrix.

The final mapped coupling matrix is obtained by weighting the geometry-defined coupling using the modal amplitudes, $J_{ij}^{\text{eff}} = \kappa_{ij}^{\text{sp}} A_i A_j$. Figure 4c shows the resulting effective coupling matrix. Compared with the bare spiral coupling, the mapped matrix more closely follows the target coupling distribution while retaining the structure imposed by the TCSEL geometry. Thus, the spiral geometry provides the interaction backbone, whereas modal-amplitude redistribution provides partial analog tunability. The agreement between the two Hamiltonians is further examined at the parameter level. Figure 4d compares the individual entries of J_{ij}^{target} and J_{ij}^{eff}. The points follow the general trend of the ideal $y = x$ line, indicating that the amplitude-mediated mapping preserves the dominant pairwise-interaction structure. Deviations arise from the geometry-defined nature of κ_{ij}^{sp}, finite amplitude tunability, and the device-level perturbations included in the model.

A similar comparison is presented for the local-field terms in Fig. 4e. The target local field h_i^{target} is compared with the mapped value h_i^{eff}, representing the effective modal bias $g_i - \gamma_i$. The distribution around the ideal trend indicates that the gain–loss-based local field reproduces the intended single-spin bias with moderate deviation. Together, these comparisons show that the mapped Hamiltonian captures both the pairwise interaction and local-bias terms.

The similarity between the target and mapped Hamiltonians is also reflected in their energy landscapes. Figure 5a compares the energy distributions over the complete 2^{16} configuration space. The distributions show substantial overlap, indicating that the mapped model preserves the global structure of the target energy landscape rather than matching only a single ground-state configuration. This is important because Ising optimization depends on the structure of the low-energy landscape as well as the final minimum-energy state.

Figures 5b and 5c show the numerical stochastic-relaxation trajectories of the target and TCSEL-mapped Hamiltonians, respectively. The thin curves represent individual runs initialized from different random spin configurations, while the thick curves show the mean energy evolution. The target system exhibits a progressive reduction in energy and converges toward its low-energy states. The TCSEL-mapped Hamiltonian shows a comparable convergence trend, although it reaches a slightly different final energy because of the coupling and local-field deviations.

Overall, the spin-state, parameter-correlation, and energy-landscape results show that the measurement-informed TCSEL Hamiltonian approximates the reference Ising model while remaining constrained by the device-native interaction structure. The model therefore preserves the relevant low-energy behavior without implying exact realization of an arbitrary target Hamiltonian.

5.3 Monte Carlo Analyses

Process variations and operating fluctuations are unavoidable in physical Ising machines. In the proposed spiral-TCSEL platform, deviations may arise from fabrication-induced aperture changes, modal-overlap uncertainty, thermal drift, gain fluctuations, and imperfect control of modal amplitudes and local fields. Because the effective coupling depends on both the geometry-defined term κ_{ij} and the tunable amplitudes A_iA_j, these perturbations can alter the mapped Hamiltonian. Monte Carlo simulations were therefore performed for $N = 16$ spins using 100 trials at each operating condition. The coupling mismatch and local-field control parameter h were varied, where larger h indicates more accurate realization of the target field through $g_i - \gamma_i$, while a fixed device-noise level of 0.08 represented residual coupling and local-field perturbations. Robustness was evaluated using the near-ground-state success rate and average spin agreement.

Figure 6a shows that the near-ground-state success rate is high at low coupling mismatch, indicating robust operation when the target problem remains close to the TCSEL-native coupling family. As the mismatch increases, the success rate decreases because amplitude weighting cannot fully compensate for deviations between the geometry-defined coupling κ_{ij} and the target interaction matrix. Nevertheless, the mapped model continues to recover useful low-energy solutions at higher mismatch levels.

Figure 6b shows that the average spin agreement remains close to or above 90% for most moderate-mismatch cases. Its weak dependence on h indicates that coupling mismatch is the dominant source of error rather than imperfect local-field control. Together, these results demonstrate that the spiral-TCSEL mapping remains tolerant

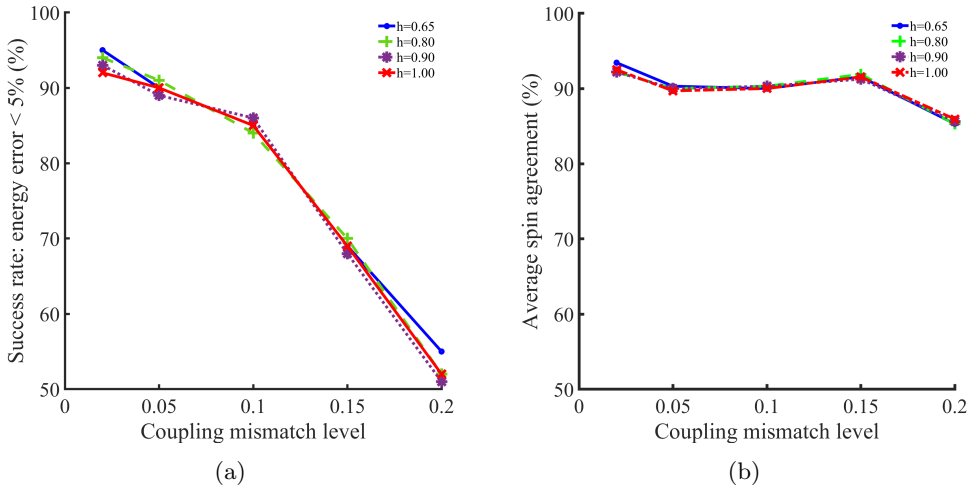

Fig. 6: Monte Carlo robustness analysis of the TCSEL-mapped Hamiltonian. (a) Near-ground-state success rate as a function of coupling mismatch and local-field control. (b) Corresponding average spin agreement with the target ground-state configuration. Each point represents 100 independent trials with a fixed device-noise level of 0.08.

to realistic parameter variations and preserves near-ground-state behavior even when the effective Hamiltonian does not exactly reproduce the target model.

5.4 Benchmarking

To evaluate the computational capability of the proposed TCSEL-based Ising solver, three representative combinatorial optimization problems are considered: Max-Cut, number partitioning, and QUBO. Max-Cut evaluates the solver's ability to identify an optimal partition of a weighted graph and therefore directly tests the implementation of pairwise spin couplings [38]. Number partitioning examines whether the system can distribute nonuniform numerical values between two subsets while minimizing their difference, thereby testing solution accuracy under heterogeneous problem coefficients [39]. QUBO provides a general framework for representing binary combinatorial optimization problems [37]. In particular, the selected QUBO instance contains both positive and negative coefficients and is therefore used to assess whether the TCSEL-mapped Hamiltonian can represent mixed-sign couplings and local biases while converging toward the correct binary solution [5, 37]. Together, these benchmarks evaluate the proposed solver across graph-partitioning, numerical-balancing, and general binary-optimization problems.

5.4.1 Max-Cut

The Max-Cut benchmark was evaluated using a 16-spin weighted graph. The target Ising Hamiltonian reached the exact Max-Cut value of 25.0392, corresponding to

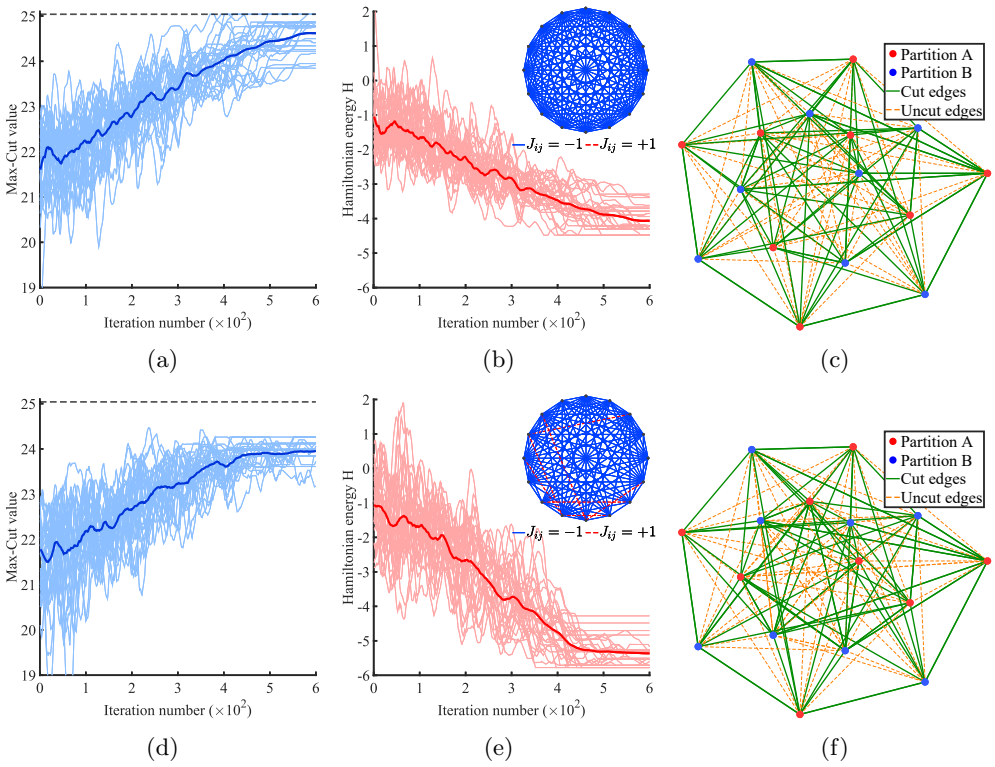

Fig. 7: Max-Cut benchmarking of the target Ising and TCSEL-mapped Hamiltonians. (a)–(c) Target Ising model and (d)–(f) TCSEL-mapped model. (a,d) Evolution of the Max-Cut value over stochastic-annealing iterations; thin curves represent individual runs, thick curves show the mean, and the dashed line indicates the optimal cut value. (b,e) Corresponding Hamiltonian-energy relaxation trajectories, with insets showing the signed coupling networks ($J_{ij} = -1$, blue; $J_{ij} = +1$, red). (c,f) Graph partitions, where red and blue nodes denote partitions A and B, respectively; green solid lines indicate cut edges, and orange dashed lines indicate uncut edges.

an approximation ratio of 100%. The TCSEL-mapped Hamiltonian achieved a cut value of 24.2624, yielding an approximation ratio of 96.90%. Although the mapped spin configuration showed a 62.50% agreement with the exact target configuration, it retained most of the optimal objective value. This result indicates that the TCSEL-mapped solver can recover a high-quality near-optimal partition despite deviations between the target and physically realizable coupling matrices. The lower spin agreement does not imply an equivalent reduction in optimization quality because different spin assignments can produce similar cut values.

Figure 7 compares the stochastic-annealing behavior of the target and TCSEL-mapped Hamiltonians. Figures 7a and 7d show that the Max-Cut objective increases during relaxation, with the target model reaching the exact optimum and

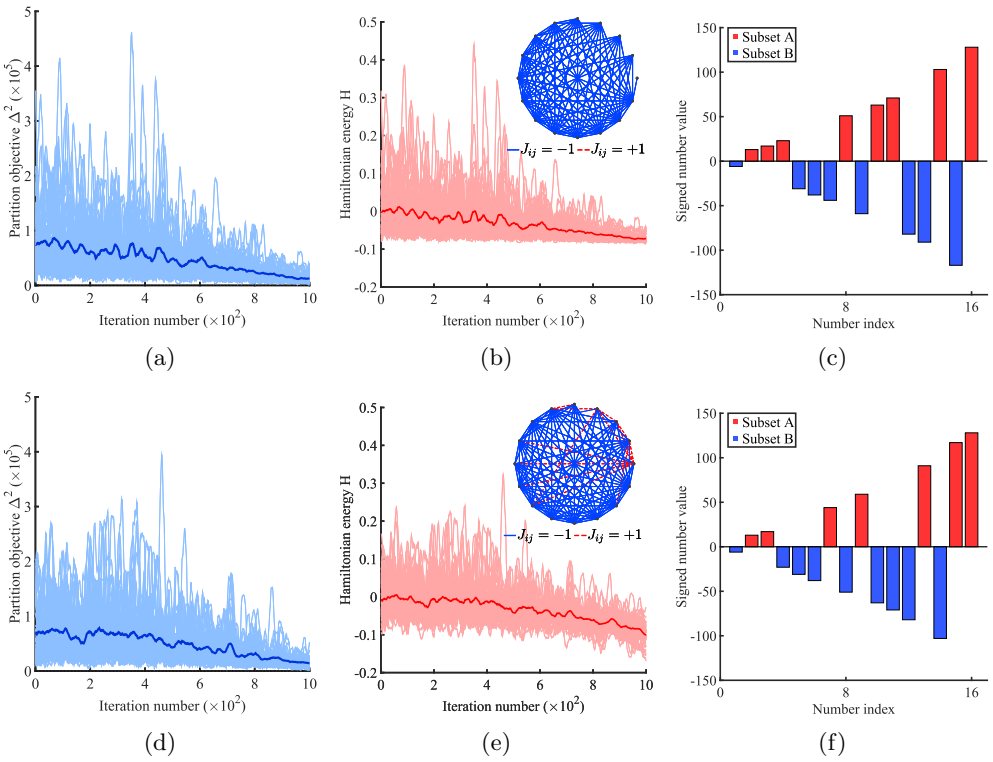

Fig. 8: Number-partitioning benchmark of the target Ising and TCSEL-mapped Hamiltonians. (a)–(c) Target Ising model and (d)–(f) TCSEL-mapped model. (a,d) Evolution of the partition objective Δ^2 during stochastic annealing; thin curves represent individual runs, while thick curves show the mean. (b,e) Corresponding Hamiltonian-energy relaxation trajectories, with insets showing the signed coupling networks ($J_{ij} = -1$, blue; $J_{ij} = +1$, red). (c,f) Final number partitions, where red positive bars denote subset A and blue negative bars denote subset B.

the mapped model converging close to it. The corresponding energy trajectories in Figs. 7b and 7e decrease toward stable low-energy states, confirming consistent Ising relaxation in both cases. The final graph partitions in Figs. 7c and 7f show differences in the assigned node states; however, the mapped solution preserves nearly all of the optimal cut weight, as reflected by its 96.90% approximation ratio.

5.4.2 Number Partitioning

The number-partitioning benchmark was evaluated using 16 integers with a total sum of 937. Because the total sum is odd, the minimum possible imbalance is $\Delta = 1$, corresponding to the exact objective value $\Delta^2 = 1$. Both the target and TCSEL-mapped Hamiltonians reached this optimum, producing partition sums of 469 and 468. Accordingly, both models achieved a normalized imbalance of 0.1067% and a

relative objective gap of 0%. The target and mapped spin agreements with the selected exact solution were 50.00% and 56.25%, respectively. These relatively low values do not indicate poor optimization performance because multiple spin configurations can yield the same optimal partition imbalance, while a global spin inversion simply exchanges the two subsets without changing the objective value.

Figure 8 compares the stochastic-annealing behavior of the target and TCSEL-mapped models. Figures 8a and 8d show that both partition objectives converge to the exact minimum $\Delta^2 = 1$. The corresponding Hamiltonian-energy trajectories in Figs. 8b and 8e decrease toward stable low-energy states, confirming successful relaxation in both cases. Although the target coupling network contains 120 negative couplings, whereas the mapped network contains 100 negative and 20 positive couplings, the TCSEL-mapped model still preserves the optimal partitioning result. The final partitions shown in Figs. 8c and 8f both produce subset sums of 469 and 468, demonstrating exact recovery of the optimal number partition despite differences in the underlying spin assignments and coupling signs.

5.4.3 Quadratic Unconstrained Binary Optimization

The planted-QUBO benchmark was evaluated using 16 binary variables with both positive and negative coupling coefficients. The planted solution coincides with the exact optimum, with a QUBO objective value of -2.5792. The target Hamiltonian recovered this solution exactly, producing a 0% relative objective gap, 100% binary-state agreement, and a Hamming distance of zero. The TCSEL-mapped Hamiltonian achieved an objective value of -2.1083, corresponding to a relative objective gap of 18.26%. Its solution agreed with the exact and planted solutions for 87.50% of the variables, with a Hamming distance of two. The target and mapped minimum Ising energies were -3.3475 and -2.8908, respectively. These results indicate that the mapped solver preserves most of the optimal binary configuration despite physical deviations in the implemented Hamiltonian.

Figure 9 compares the stochastic-annealing behavior of the target and TCSEL-mapped QUBO models. Figures 9a and 9d show that the target objective converges to the exact optimum, whereas the mapped objective approaches a nearby solution. The corresponding energy trajectories in Figs. 9b and 9e decrease toward stable low-energy states, demonstrating successful relaxation in both cases. The target coupling network contains 64 positive and 56 negative couplings, while the mapped network contains 61 positive and 59 negative couplings, showing that the TCSEL mapping largely preserves the mixed-sign interaction structure. As shown in Figs. 9c and 9f, the target solver exactly reproduces the optimal binary vector, while the mapped solution differs at only two variable positions.

5.5 Comparison

We compare the proposed spiral-TCSEL-based Ising substrate with representative state-of-the-art Ising-machine implementations, including CMOS oscillator-based [10], spintronic [12], quantum-annealing platforms [13], and coherent photonic [16]. The purpose of this comparison is not to suggest that the present device exceeds established

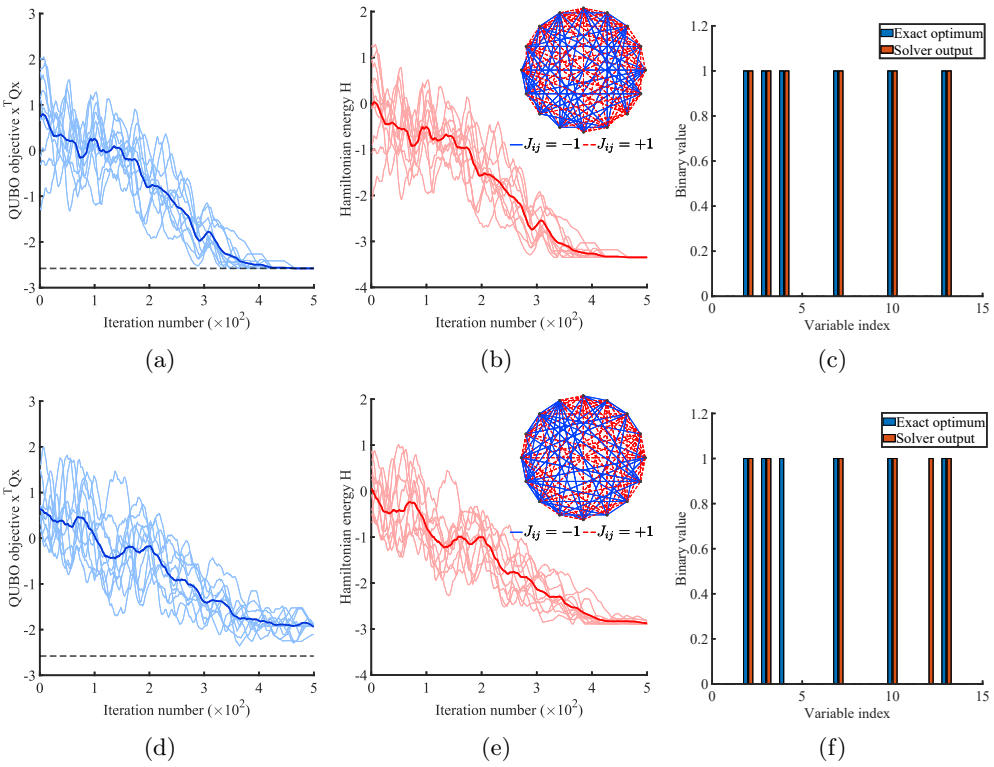

Fig. 9: QUBO benchmarking of the target Ising and TCSEL-mapped Hamiltonians. (a)–(c) Target Ising model and (d)–(f) TCSEL-mapped model. (a,d) Evolution of the QUBO objective during stochastic annealing; thin curves represent individual runs, the thick curve shows the mean, and the dashed line indicates the optimal objective value. (b,e) Corresponding Hamiltonian-energy relaxation trajectories, with insets showing the signed coupling networks ($J_{ij} = -1$, blue; $J_{ij} = +1$, red). (c,f) Comparison between the exact optimal binary solution and the solver output across the variable indices.

large-scale Ising machines in total spin count, but to assess its device-level integration characteristics relative to representative physical solvers.

A direct comparison requires consideration of the physical unit used to represent each spin. In many existing platforms, one spin is represented by one oscillator, optical pulse, magnetic tunnel junction, or superconducting qubit. In contrast, the proposed approach represents multiple effective spins within a single spiral-TCSEL cavity through its transverse optical degrees of freedom. Table 2 therefore compares the total demonstrated scale, effective spins per physical unit, coupling mechanism, and operating condition.

In terms of total problem size, the present $N = 16$ benchmark is smaller than large-scale CMOS, coherent-photonic, spintronic, and quantum-annealing

Table 2: Comparison with representative Ising-machine implementations

Platform	Physical unit	Total scale	Spins per unit	Operation
CMOS Ising Chip [10]	Oscillator node	1,968 nodes	1	Room-temperature CMOS
SMTJ Ising Annealer [12]	SMTJ device	80 SMTJs	1	Room temperature
D-Wave Advantage [13]	Superconducting qubit	5,640 qubits	1	Cryogenic quantum annealing
Coherent Ising Machine [16]	Optical pulse	100,512 spins	1	Time-multiplexed optics
TCSEL Ising	Coupled-cavity TCSEL	16 effective spins	16	Room-temperature photonic relaxation

implementations. These established platforms have demonstrated systems ranging from tens to more than 10^5 physical or effective spin variables and are therefore more mature for large-scale programmable optimization. Their scaling, however, generally relies on increasing the number of physical units, time-multiplexing optical pulses, implementing electrical interconnects, or expanding cryogenic qubit networks.

The normalized comparison highlights the distinguishing feature of the spiral-TCSEL approach. The present mapping represents 16 effective optical spins within one TCSEL cavity, whereas the compared platforms generally assign one spin to each oscillator node, optical pulse, SMTJ device, or superconducting qubit. This device-level spin density is enabled by the multimode transverse response of the spiral aperture, for which the same physical cavity provides the optical degrees of freedom and the geometry-defined interaction backbone.

The implementations also differ in how their interactions are realized. Coherent Ising machines typically use time-multiplexed optical systems and measurement-feedback infrastructure, while quantum annealers require cryogenic operation and graph embedding. In the proposed approach, the interaction backbone is associated with the spiral geometry and modal overlap, while modal amplitudes and the gain–loss landscape provide partial analog tunability. This reduces the number of replicated physical units required for the present 16-spin representation.

The present results demonstrate the feasibility of using a single spiral-TCSEL cavity as a compact, measurement-informed Ising-like substrate. Although the current numerical benchmark contains only 16 effective spins, these spins are represented within one photonic device rather than across 16 replicated optical units. The geometry-defined coupling provides a fixed interaction backbone, while modal-amplitude redistribution provides partial tunability of the effective Hamiltonian. Larger implementations may be pursued through increased modal resolution, engineered spiral geometries, or arrays of coupled TCSEL devices.

6 Conclusion

In this paper, we introduced SPIRA, a measurement-informed photonic Ising relaxation architecture based on the multimode response of a fabricated spiral-aperture TCSEL. The device was experimentally characterized through multimode emission spectra, current-dependent optical-output measurements, and temperature-dependent near-field intensity distributions. These measurements were used to identify the effective optical sites and extract the modal amplitudes required to construct a 16-spin effective Hamiltonian. In the proposed mapping, the spiral geometry and modal overlap define the device-native interaction backbone, the experimentally extracted amplitudes weight the effective couplings, and the local fields are represented through mode-dependent gain–loss imbalance.

The resulting measurement-informed TCSEL Hamiltonian achieved a ground-state spin agreement of 87.50% and a relative energy error of 6.42% with respect to the target Ising Hamiltonian. Despite relative coupling and local-field errors of 34.21% and 23.69%, respectively, the mapped model preserved the dominant low-energy structure of the target problem. Monte Carlo analysis further showed that the near-ground-state success rate and average spin agreement remain robust under moderate coupling mismatch, local-field uncertainty, and device-level perturbations, demonstrating the tolerance of the measurement-informed mapping to realistic variations in the optical parameters.

The computational benchmarks further demonstrated the optimization capability of the experimentally constrained Hamiltonian. The TCSEL-mapped model achieved 96.90% of the exact Max-Cut objective, recovered the optimal number-partitioning solution with zero objective gap, and reproduced 87.50% of the optimal QUBO variables with a relative objective gap of 18.26%. These results show that the measured modal-amplitude distribution and geometry-defined coupling structure can preserve high-quality optimization solutions even when the effective Hamiltonian does not exactly reproduce the target coupling and local-field parameters.

The principal contribution of SPIRA is the representation of multiple effective spins and their interactions within a single measured semiconductor laser device rather than through replicated optical units. The present experiments directly establish the multimode optical response and temperature-dependent amplitude redistribution used in the Ising mapping, while the binary phase states and relaxation trajectories are evaluated numerically within the resulting measurement-informed Hamiltonian. Future work will focus on phase-resolved optical measurements for direct experimental spin readout, mode-dependent gain–loss calibration, dynamic electrical and thermal annealing, engineered spiral geometries with improved coupling programmability, and scaling through increased modal density and coupled spiral-TCSEL arrays.

Funding. The authors received no funding for this research.

Data availability. The data supporting the findings of this study are available from the corresponding author upon reasonable request.

Competing interests. The authors declare no competing interests.

Author contributions. S.A. performed the experimental measurements, experimental characterization, Hamiltonian construction, and numerical analysis. A.A. performed the image processing, developed the reduced dynamical model, and contributed to the computational evaluation. M.K.Q.J. contributed to the optimization formulation and benchmark analysis. L.G., P.K., J.T., and J.G. contributed to the device design, fabrication, and physical interpretation. E.J.D. contributed to the optimization methodology and numerical validation. H.D. conceived and supervised the project, developed the spiral-TCSEL concept, directed the theoretical and experimental investigations, and coordinated the preparation of the manuscript. All authors analyzed the results, revised the manuscript, and approved the final version.

References

[1] Wang, R.Z., Cummins, J.S., Syed, M., Stroev, N., Pastras, G., Sakellariou, J., Tsintzos, S., Askitopoulos, A., Veraldi, D., Calvanese Strinati, M., Gentilini, S., Pierangeli, D., Conti, C., Berloff, N.G.: Efficient computation using spatial-photonic ising machines with low-rank and circulant matrix constraints. Communications Physics **8**, 86 (2025) https://doi.org/10.1038/s42005-025-01987-5

[2] Karp, R.M.: Reducibility among combinatorial problems. In: Miller, R.E., Thatcher, J.W. (eds.) Complexity of Computer Computations, pp. 85–103. Plenum Press, New York (1972). https://doi.org/10.1007/978-1-4684-2001-2_9

[3] Glover, F., Kochenberger, G., Du, Y.: Quantum bridge analytics i: a tutorial on formulating and using qubo models. 4OR **17**, 335–371 (2019) https://doi.org/10.1007/s10288-019-00424-y

[4] Barahona, F.: On the computational complexity of ising spin glass models. Journal of Physics A: Mathematical and General **15**(10), 3241–3253 (1982) https://doi.org/10.1088/0305-4470/15/10/028

[5] Lucas, A.: Ising formulations of many np problems. Frontiers in Physics **2**, 5 (2014) https://doi.org/10.3389/fphy.2014.00005

[6] Mohseni, N., McMahon, P.L., Byrnes, T.: Ising machines as hardware solvers of combinatorial optimization problems. Nature Reviews Physics **4**(6), 363–379 (2022) https://doi.org/10.1038/s42254-022-00440-8

[7] Gao, Y., Chen, G., Qi, L., Fu, W., Yuan, Z., Danner, A.J.: Photonic ising machines for combinatorial optimization problems. Applied Physics Reviews **11**(4), 041307 (2024) https://doi.org/10.1063/5.0216656

[8] Ouyang, J., Liao, Y., Ma, Z., Kong, D., Feng, X., Zhang, X., Dong, X., Cui, K., Liu, F., Zhang, W., Huang, Y.: On-demand photonic ising machine with simplified hamiltonian calculation by phase encoding and intensity

detection. Communications Physics **7**, 168 (2024) https://doi.org/10.1038/s42005-024-01658-x

[9] Yamaoka, M., Yoshimura, C., Hayashi, M., Okuyama, T., Aoki, H., Mizuno, H.: A 20k-spin ising chip to solve combinatorial optimization problems with cmos annealing. IEEE Journal of Solid-State Circuits **51**(1), 303–309 (2016) https://doi.org/10.1109/JSSC.2015.2498601

[10] Moy, W.G., Ahmed, I., Chiu, P.-w., Moy, J., Sapatnekar, S.S., Kim, C.H.: A 1,968-node coupled ring oscillator circuit for combinatorial optimization problem solving. Nature Electronics **5**(5), 310–317 (2022) https://doi.org/10.1038/s41928-022-00749-3

[11] Garg, C., Salahuddin, S.: Efficient optimization accelerator framework for multi-state spin ising problems. Nature Communications **16**, 9601 (2025) https://doi.org/10.1038/s41467-025-64625-2

[12] Si, J., Yang, S., Cen, Y., Chen, J., Yao, Z., Kim, D.-J., Cai, K., Yoo, J., Fong, X., Yang, H.: Energy-efficient superparamagnetic ising machine and its application to traveling salesman problems. Nature Communications **15**(3457) (2024) https://doi.org/10.1038/s41467-024-47818-z

[13] D-Wave Systems: D-Wave Quantum Computing Products: Topologies. Online documentation (2024). https://docs.dwavequantum.com/en/latest/quantum_research/topologies.html

[14] McMahon, P.L., Marandi, A., Haribara, Y., Hamerly, R., Langrock, C., Tamate, S., Inagaki, T., Takesue, H., Utsunomiya, S., Aihara, K., Byer, R.L., Fejer, M.M., Mabuchi, H., Yamamoto, Y.: A fully programmable 100-spin coherent ising machine with all-to-all connections. Science **354**(6312), 614–617 (2016) https://doi.org/10.1126/science.aah5178

[15] Inagaki, T., Haribara, Y., Igarashi, K., Sonobe, T., Tamate, S., Honjo, T., Marandi, A., McMahon, P.L., Umeki, T., Enbutsu, K., Tadanaga, O., Takenouchi, H., Aihara, K., Kawarabayashi, K.-i., Inoue, K., Utsunomiya, S., Takesue, H.: A coherent ising machine for 2000-node optimization problems. Science **354**(6312), 603–606 (2016) https://doi.org/10.1126/science.aah4243

[16] Honjo, T., Sonobe, T., Inaba, K., Inagaki, T., Ikuta, T., Yamada, Y., Kazama, T., Enbutsu, K., Umeki, T., Kasahara, R., Kawarabayashi, K.-i., Takesue, H.: 100,000-spin coherent ising machine. Science Advances **7**(40), 0952 (2021) https://doi.org/10.1126/sciadv.abh0952

[17] Al-Kayed, N., St-Arnault, C., Morison, H., Aadhi, A., Huang, C., Tait, A.N., Plant, D.V., Shastri, B.J.: Programmable 200 gops hopfield-inspired photonic ising machine. Nature **648**, 576–584 (2025) https://doi.org/10.1038/s41586-025-09838-7

[18] Wu, B., Zhang, W., Zhang, S., Zhou, H., Ruan, Z., Li, M., Huang, D., Dong, J., Zhang, X.: A monolithically integrated optical ising machine. Nature Communications **16**, 4296 (2025) https://doi.org/10.1038/s41467-025-59537-0

[19] Hu, Z., Ren, Y., Meng, Y., Wang, T., Jiang, Y., Wei, M., Xiao, Y., Li, Z., Li, M.: Programmable optoelectronic ising machine for optimization of real-world problems. Light: Science & Applications **15**, 6 (2026) https://doi.org/10.1038/s41377-025-02100-9

[20] Sakellariou, J., Askitopoulos, A., Pastras, G., Tsintzos, S.I.: Encoding arbitrary ising hamiltonians on spatial photonic ising machines. Physical Review Letters **134**(20), 203801 (2025) https://doi.org/10.1103/PhysRevLett.134.203801

[21] Skalli, A., Robertson, J., Owen-Newns, D., Hejda, M., Porte, X., Reitzenstein, S., Hurtado, A., Brunner, D.: Photonic neuromorphic computing using vertical cavity semiconductor lasers. Optical Materials Express **12**(6), 2395–2414 (2022) https://doi.org/10.1364/OME.450926

[22] Pan, G., *et al.*: Harnessing the capabilities of vcsels: unlocking the potential for advanced integrated photonic devices and systems. Light: Science & Applications **13**, 290 (2024) https://doi.org/10.1038/s41377-024-01561-8

[23] Giudici, M., Green, C., Giacomelli, G., Nespolo, U., Tredicce, J.R.: Polarization dynamics in vertical-cavity surface-emitting lasers with optical feedback. Journal of the Optical Society of America B **16**(11), 2114–2123 (1999) https://doi.org/10.1364/JOSAB.16.002114

[24] Panajotov, K., Sciamanna, M., Gatare, I., Arteaga, M., Thienpont, H.: Nonlinear dynamics of vertical-cavity surface-emitting lasers. Advances in Optical Technologies **2011**, 469627 (2011) https://doi.org/10.1155/2011/469627

[25] Bittner, S., Sciamanna, M.: Complex nonlinear dynamics of polarization and transverse modes in a broad-area vertical-cavity surface-emitting laser. APL Photonics **7**(12), 126108 (2022) https://doi.org/10.1063/5.0104852

[26] Degen, C., Fischer, I., Elsäßer, W.: Transverse modes in oxide confined vcsels: Influence of pump profile, spatial hole burning, and thermal effects. Optics Express **5**(3), 38–47 (1999) https://doi.org/10.1364/OE.5.000038

[27] Hu, S., Li, Z., Lee, C., Li, X., Tian, B., Zhu, L., Xin, X.: Transverse-mode control in vcsel with an intra-cavity metalens. Optics Express **33**(11), 23156–23167 (2025) https://doi.org/10.1364/OE.557095

[28] Larsson, A.: Advances in vcsels for communication and sensing. IEEE Journal of Selected Topics in Quantum Electronics **17**(6), 1552–1567 (2011) https://doi.org/10.1109/JSTQE.2011.2119469

[29] Westbergh, P., Safaisini, R., Haglund, E., Kögel, B., Gustavsson, J.S., Larsson, A., Geen, M., Lawrence, R., Joel, A.: High-speed 850 nm vcsels operating error free up to 47 gbit/s. Electronics Letters **48**(18), 1145–1147 (2012) https://doi.org/10.1049/el.2012.2525

[30] Hu, S., Zhang, X., Li, C., Yin, H., Li, X., Xin, X.: Latest advances in vcsel technology for next-generation data center network [invited]. Chinese Optics Letters **22**(11), 111401 (2024) https://doi.org/10.3788/COL202422.111401

[31] Dalir, H., Koyama, F.: 29 ghz directly modulated 980 nm vertical-cavity surface emitting lasers with bow-tie shape transverse coupled cavity. Applied Physics Letters **103**(9), 091109 (2013) https://doi.org/10.1063/1.4820149

[32] Dalir, H., Koyama, F.: Highly stable operations of transverse coupled cavity vcsels with enhanced modulation bandwidth. Electronics Letters **50**(11), 823–824 (2014) https://doi.org/10.1049/el.2014.0900

[33] Heidari, E., Dalir, H., Ahmed, M., Sorger, V.J., Chen, R.T.: Hexagonal transverse-coupled-cavity vcsel redefining the high-speed lasers. Nanophotonics **9**(13), 4389–4395 (2020) https://doi.org/10.1515/nanoph-2020-0437

[34] Dalir, H., Koyama, F.: 30ghz ultracompact electroabsorption modulator integrated with 980nm vcsel with resonance effect in coupled cavities. Applied Physics Express **7**(11), 112101 (2014) https://doi.org/10.7567/APEX.7.112101

[35] Dalir, H., Takahashi, Y., Koyama, F.: Low-voltage, high-speed and compact electro-absorption modulator laterally integrated with 980-nm vcsel. Optics Express **22**(21), 25746–25755 (2014) https://doi.org/10.1364/OE.22.025746

[36] Wu, T., Cai, Q., Jahannia, B., Patil, C., Ye, J., Ahmadian, M., Dalir, H., Heidari, E.: Tunable laser using transverse cavity surface emitting laser working near exceptional point. ACS Photonics **12**(4), 1754–1762 (2025) https://doi.org/10.1021/acsphotonics.5c00006

[37] Glover, F., Kochenberger, G., Hennig, R., Du, Y.: Quantum bridge analytics i: A tutorial on formulating and using qubo models. Annals of Operations Research **314**(1), 141–183 (2022) https://doi.org/10.1007/s10479-022-04634-2

[38] Goemans, M.X., Williamson, D.P.: Improved approximation algorithms for maximum cut and satisfiability problems using semidefinite programming. Journal of the ACM **42**(6), 1115–1145 (1995) https://doi.org/10.1145/227683.227684

[39] Mertens, S.: The easiest hard problem: Number partitioning. In: Percus, A.G., Istrate, G., Moore, C. (eds.) Computational Complexity and Statistical Physics, pp. 125–139. Oxford University Press, ??? (2006). https://doi.org/10.1093/oso/9780195177374.003.0012